Heat-Induced Liquid Hovering in Liquid-Gas Coexistence under Gravity

Akira Yoshida[*] and Naoko Nakagawa[†]

Department of Physics, Ibaraki University, Mito 310-8512, Japan

Shin-ichi Sasa[‡]

Department of Physics, Kyoto University, Kyoto 606-8502, Japan

We study a liquid-gas coexistence system in a container under gravity with heat flow in the direction opposite to gravity. By molecular dynamics simulation, we find that the liquid buoys up and continues to float steadily. The height at which the liquid floats is determined by a dimensionless parameter related to the ratio of the temperature gradient to gravity. We confirm that supercooled gas remains stable above the liquid. We provide a phenomenological argument for explaining the phenomenon from a simple thermodynamic assumption.

Introduction—Clouds float in the sky although they are heavier than the surface air. According to the standard theory, thermal convection caused by the temperature difference between the sea surface and the atmosphere forms cumulonimbus clouds hovering over the sea [1–3]. While cloud formation may involve various complex processes, convection certainly plays a significant role in this phenomenon. The Leidenfrost effect is another phenomenon of a liquid floating above a gas [4–7]. When we drop a droplet onto a hot plate, heat transfers violently from the plate to the droplet. The droplet then evaporates instantly, and the vapor envelops the droplets and causes them to float. Even in this case, a complex flow of materials appears.

Motivated by these phenomena, we investigate the possibility that a liquid can float over a gas against gravity when a heat flux is imposed without convection. In equilibrium phase coexistence under gravity, a phase with a higher mass density is located below a phase with a lower mass density. Supposing that the phase with a higher mass density is preferable at low temperatures, such as a liquid phase in liquid-gas coexistence, a somewhat frustrating situation occurs when the heat flux is imposed against gravity. Therefore, it might be possible that the liquid floats over the gas against gravity.

In this Letter, we explore the phenomenon through molecular dynamics simulations. We find that when the directions of the gravitational force and the heat flux are opposite to each other, the liquid floats over the gas. No convection occurs, but a persistent heat flux generates an extra force balanced with gravity. The height of the floating

liquid is characterized by a dimensionless parameter that represents the ratio of the temperature gradient to gravity. This scaling relation enables us to quantitatively predict the height of the floating liquid in a real experimental setup. Furthermore, we show that if a steady state is realized in the setup, there should be a region where the metastable states at equilibrium become stable under gravity and heat flow. In particular, the liquid floats only when the gas in the low-temperature region is supercooled at equilibrium.

Setup—Liquid-gas transition occurs universally for any molecular system and even for noble gases without electric interactions. The noble gases have been modeled as simple systems using a Lennard-Jones potential, which is suitable for numerically studying various dynamic behaviors led by transitions [8–22]. In our numerical simulations, we confine N particles in a rectangular container with a height L_x and side lengths L_y and L_z, or height L_x and side length L_y in two-dimensional cases, under gravity. For a collection of particle positions and momenta, $\Gamma = (\mathbf{r}_1, \mathbf{r}_2, \ldots, \mathbf{r}_N, \mathbf{p}_1, \mathbf{p}_2, \ldots, \mathbf{p}_N)$, we assume the Hamiltonian as

$$H(\Gamma) = \sum_i \left[\frac{|\mathbf{p}_i|^2}{2m} + \sum_{j<i} \phi(|\mathbf{r}_i - \mathbf{r}_j|) + mgx_i + V_{\text{wall}}(\mathbf{r}_i) \right],$$
(1)

where m is the mass of the particles, and g is the gravitational acceleration. The two-body interaction potential ϕ is the 12-6 Lennard-Jones interaction

$$\phi(r) = 4\varepsilon \left[\left(\frac{\sigma}{r} \right)^{12} - \left(\frac{\sigma}{r} \right)^6 \right] \theta(r_c - r).$$
(2)

Here, r is the distance between two particles, ε is the well depth, σ is the particle diameter, r_c is the cutoff length of the

---

[*]Contact author: a.yoshida.phys@gmail.com
[†]Contact author: naoko.nakagawa.phys@vc.ibaraki.ac.jp
[‡]Contact author: sasa.shinichi.6n@kyoto-u.ac.jp

interaction, and $\theta(r_c - r)$ is the Heaviside step function. In the simulations, we set the cutoff length as $r_c = 3\sigma$. We assume a fixed boundary condition at $x = 0$ and $x = L_x$ using a soft-core repulsive wall represented by $V_{\text{wall}}(\boldsymbol{r}_i)$, where we adopt the Weeks-Chandler-Andersen potential to truncate the attracting interaction in (2) [23]. Other boundaries in the y and z directions are periodic.

The container is in contact with two heat baths at the top and bottom. To represent this setup, we perform molecular dynamics simulations with Langevin thermostats having two temperatures T_H and T_C. Each molecule evolves according to

$$\dot{\boldsymbol{p}}_i = -\frac{\partial H}{\partial \boldsymbol{r}_i} - \frac{\gamma(x_i)}{m}\boldsymbol{p}_i + \sqrt{2\gamma(x_i)k_B T_b(x_i)}\boldsymbol{\xi}_i(t), \quad (3)$$

with $\dot{\boldsymbol{r}}_i = \boldsymbol{p}_i/m_i$, where $\gamma(x_i) = 1$ and $T_b(x_i) = T_H$ in the region $0 < x_i < 8\sigma$, $\gamma(x_i) = 1$ and $T_b(x_i) = T_C$ in the region $L_x - 8\sigma < x_i < L_x$, and $\gamma(x_i) = 0$ in $8\sigma \leq x_i \leq L_x - 8\sigma$. $\boldsymbol{\xi}_i(t) = (\xi_i^x(t), \xi_i^y(t), \xi_i^z(t))$ is Gaussian white noise that satisfies $\langle \xi_i^a(t) \rangle = 0$ and $\langle \xi_i^a(t)\xi_j^b(t') \rangle = \delta_{i,j}\delta_{a,b}\delta(t - t')$, where a and b are x, y, or z. We study the cases where T_H and T_C are far below the critical point and far above the crystallization temperature. The width of the thermostatted region, 8σ, is sufficiently large compared to the mean free path in the liquid but comparable in the gas. For later convenience, we define the middle temperature as $T_m = (T_H + T_C)/2$ and the temperature difference as $\Delta T = T_H - T_C$.

Observation—We first prepared the equilibrium liquid-gas coexistence under gravity. We set the mean number density $N/(L_x L_y L_z)$ and the temperature T_m so that the volume ratio of the gas and liquid was almost 1. Figure 1(a) shows a typical configuration after sufficient relaxation for the system with the aspect ratio $L_x : L_y : L_z = 4 : 1 : 1$ for $\Delta T = 0$. We see that the dense liquid is located in the lower region owing to gravity.

We then changed the values of T_H and T_C with $k_B\Delta T = 0.1\varepsilon$ while keeping the temperature T at the middle value. Starting from the equilibrium state in Fig. 1(a), we find that the bulk of the liquid floats up gradually without separating into drops and then keeps hovering as shown in a snapshot of the particle configuration in Fig. 1(b). The relaxation process to a floating state is also shown in [24].

To characterize the steady state, we calculated the number density per unit volume and the temperature profiles

$$\rho(x) = \frac{\sum_i \langle \delta(x - x_i) \rangle}{L_y L_z}, \quad T(x) = \frac{\sum_i \langle \delta(x - x_i)|\boldsymbol{p}_i|^2 \rangle}{3k_B L_y L_z m\rho(x)}, \quad (4)$$

where $\langle \cdot \rangle$ is the long-term average after the relaxation. In Fig. 2, $\rho(x)$ shows two sharp interfaces separating the liquid and gas layers. This means that the liquid layer is hovering and stationary. Correspondingly, $T(x)$ shows
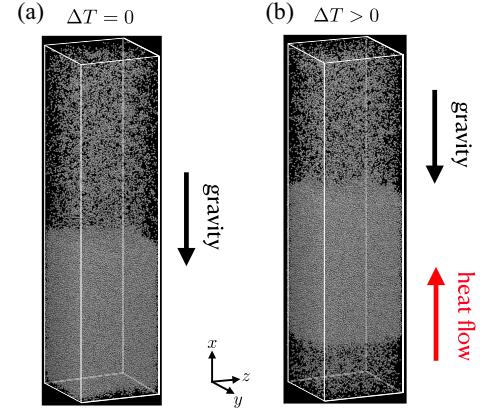

FIG. 1. Snapshots of the steady states under a gravitational force of $mg = 6.25 \times 10^{-5}\varepsilon/\sigma$, $k_B T_m = 1.0\varepsilon$, and mean density $N/L_x L_y L_z = 0.3/\sigma^3$. (a) $k_B\Delta T = 0$, (b) $k_B\Delta T = 0.1\varepsilon$. The aspect ratio is $L_x : L_y : L_z = 4 : 1 : 1$, and the system size is $L_x = 191\sigma$ corresponding to $N = 131, 072$. The width of each thermostatted region is 4.2% of L_x.

three regions with different slopes. The respective slopes result in a uniform heat current parallel to x. The local velocities in the steady hovering state suggest that there is no convection in the hot-gas layer occupying the lower region [24].

The liquid-hovering state is also observed in two-dimensional systems with $L_x : L_y = 2 : 1$. Some examples of the snapshot and the time evolution in two dimensions are displayed in [24]. Below, we concentrate on two-dimensional systems to examine the properties of the hovering state.

Condition for hovering—We confirmed that the liquid hovers stationary under gravity and heat flow by varying the parameters of the container. The details of the following examples are demonstrated in [24]. When the lateral boundary conditions are changed to be fixed, the floating liquid becomes slightly round owing to the repulsive interaction with the side walls. The liquid continues to float without separating into pieces even when the
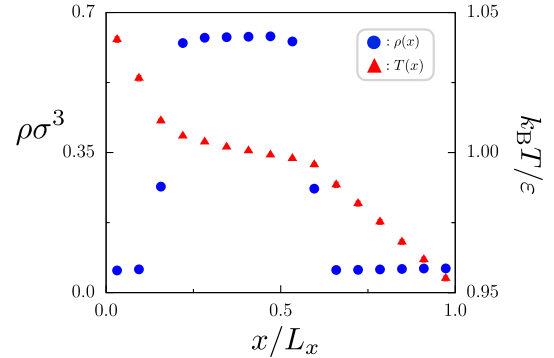

FIG. 2. Steady-state profiles of the number density $\rho(x)$ and temperature $T(x)$ for the system in Fig. 1(b) with $\chi = 8.37$. The error bars are smaller than the symbols.

container is horizontal with $L_x:L_y = 1:2$. However, when we impose wet boundary conditions using attractive interactions between each particle and the top or bottom walls, we observe that the liquid sticks to the top or bottom boundary, or exhibits nonstationary motion.

We then focused on the original boundary condition mentioned in the setup at the beginning. We took a mean density $N/(L_xL_y/\sigma^2) = 0.4$ and $k_BT_m/\varepsilon = 0.43$ such that the volume ratio of the liquid and gas was almost 1. The aspect ratio was fixed as $L_x:L_y = 2:1$. To characterize the hovering state, we examined how the center of mass

$$X = \sum_i \frac{\langle x_i \rangle}{N} \qquad (5)$$

depends on the temperature difference ΔT and the gravitational acceleration g and attempted to determine the functional form of $X(g, \Delta T)$ when $\Delta T > 0$ and $g > 0$. We calculated X for four values of $k_B\Delta T$ with changing g for $L_x = 158\sigma$ ($N = 5.0 \times 10^3$). The important result is that $X(g, \Delta T)$ can be expressed in terms of a scaling function. We first notice that the one-particle kinetic energy difference between the top and the bottom is $k_B\Delta T$. This quantity should be comparable with the potential energy difference mgL_x. We then define the dimensionless parameter

$$\chi \equiv \frac{k_B\Delta T}{mgL_x}. \qquad (6)$$

In Fig. 3, we plot $X(g, \Delta T)/L_x$ as a function of χ. We find that the data collapse on a single curve, $X = X(\chi)$. That is, the system is invariant for the transformation of $(g, \Delta T) \rightarrow (\alpha g, \alpha \Delta T)$ with any positive real α. This result implies that the temperature gradient plays the same role as the gravitational force.

To check the system size dependence, we examined $X(\chi)$ for $L_x = 632\sigma$ ($N = 8.0 \times 10^4$) fixing $k_B\Delta T = 0.04\varepsilon$ and found the slight deviation of $X(\chi)$. A point calculated in $L_x = 2371\sigma$ ($N = 1.125 \times 10^6$) also deviates from the scaling function in $L_x = 158\sigma$. We then concentrated on the case $\chi = 12.65$ and varied L_x/σ from 158 to 2372, i.e., $5.0 \times 10^3 \le N \le 1.125 \times 10^6$. See the inset of Fig. 3. Note that $X_{\min} < X < X_{\max}$, where $X_{\min}$ is the position of X when $\Delta T = 0$ for the respective value of mg, and $X_{\max} = L_x - X_{\min}$. We observe a gradual increase in X and $X_{\max}$ with L_x. The scaling function tends to converge to the dotted line representing $X(\chi)$ in the thermodynamic limit, which will be derived below.

Thermodynamics—For the system of $L_x = 632\sigma$ with $\chi = 12.65$ and $k_B\Delta T/\varepsilon = 0.04$, we first calculated $\rho(x)$, $T(x)$, and the Irving-Kirkwood stress tensor components $P_{xx}(x)$ and $P_{yy}(x)$ in the steady state [25]. Each profile is shown in [24], where the consistency in the normal stress is shown as $P_{xx}(x) = P_{yy}(x)$ except for the vicinity
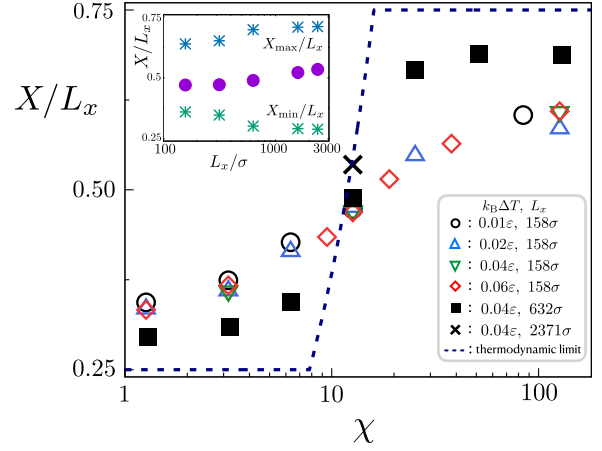

FIG. 3. Center of mass X/L_x versus $\chi = k_B\Delta T/mgL_x$. Parameter values of $(k_B\Delta T, mg, L_x)$ for calculating each point are shown in [24]. The error bars are smaller than the symbols. The points for $L_x = 2L_y = 158\sigma$ (open symbols) show the collapse $(g, \Delta T) \rightarrow (\alpha g, \alpha \Delta T)$ with four different degrees of nonequilibrium, $k_B\Delta T/\varepsilon = 0.01, 0.02, 0.04, 0.06$ at $k_BT_m/\varepsilon = 0.43$. System size dependence of the collapsed curve is examined with 632σ (filled square), 2371σ (cross), and the thermodynamic limit with (9) (dotted line). Inset: system size effects in X/L_x and $X_{\max}/L_x$ at $\chi = 12.65$ with $k_B\Delta T/\varepsilon = 0.04$. $L_x/\sigma = 158, 316, 632, 1581,$ and 2371.

of the interface. We thus define the local pressure as $P(x) \equiv P_{xx}(x)$. In Fig. 4, $\rho(x)$ and local pressure $P(x)$ are plotted simultaneously. We find that $P(x)$ is almost constant in the hot and cold gas layers.

To examine the local equilibrium properties at each x, we numerically simulated the equilibrium system with the NVT ensemble using the obtained local steady-state values $(T(x), \rho(x))$. We set $N = 8.0 \times 10^4$ at $g = 0$ with a
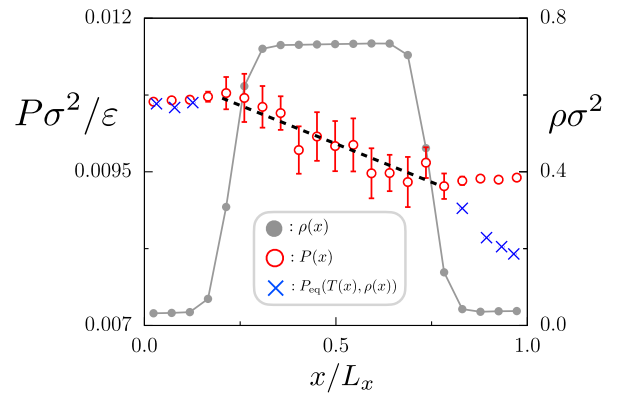

FIG. 4. Comparison of the local steady state and local equilibrium state with respect to pressure for $\chi = 12.65$, $k_B\Delta T/\varepsilon = 0.04$, $L_x = 632\sigma$, and $N = 8.0 \times 10^4$. The error bars are twice the standard deviation. The width of each thermostatted region is 1.3% of L_x. The density profile $\rho(x)$ indicates the positions of the two interfaces. The local steady pressure $P(x)$ is different from the local equilibrium pressure $P_{eq}(T(x), \rho(x))$ in the cold-gas layer.

periodic boundary condition for x and y, and calculated the virial pressure to determine the "equilibrium" pressure $P_{\mathrm{eq}}(T(x), \rho(x))$. The details of the determination of $P_{\mathrm{eq}}(T(x), \rho(x))$ are explained in [24]. Figure 4 provides a simultaneous plot of $P(x)$ and $P_{\mathrm{eq}}(T(x), \rho(x))$. We find that $P(x) \simeq P_{\mathrm{eq}}(T(x), \rho(x))$ in the hot-gas layer occupying the lower space, while $P(x) \neq P_{\mathrm{eq}}(T(x), \rho(x))$ in the cold-gas layer occupying the upper space. The difference becomes larger with increasing distance from the interface between the liquid and the cold gas. In the cold gas, the equilibrium state for $(T(x), \rho(x))$ turns into the liquid-gas coexistence. Thus, the cold gas is considered to be super-cooled, which is not equilibrium but metastable.

Scaling function in the thermodynamic limit—In Fig. 4, the two liquid-gas interfaces are in local equilibrium and therefore the pressures are saturated there. The profiles of $P(x)$ and $T(x)$ are piecewise linear. Based on these observations, the local pressure $P(x)$ in the liquid is identified as the saturation pressure $P_{\mathrm{s}}(T(x))$ for the local temperature $T(x)$ [24].

Letting the position of the interfaces be x_1^{int} and x_2^{int} with $x_1^{\mathrm{int}} < x_2^{\mathrm{int}}$, the force balance is written as

$$P_{\mathrm{s}}(T(x_1^{\mathrm{int}})) - P_{\mathrm{s}}(T(x_2^{\mathrm{int}})) = mg\rho^{\mathrm{L}}\Delta^{\mathrm{L}} \qquad (7)$$

with the width of the liquid layer $\Delta^{\mathrm{L}} \equiv x_2^{\mathrm{int}} - x_1^{\mathrm{int}}$ and the number density ρ^{L} of the liquid. Using $dP_{\mathrm{s}}/dx = (dP_{\mathrm{s}}/dT)(dT/dx)$, we extract the leading order contribution to (7) in the limit $\Delta T/T_{\mathrm{m}} \to 0$. We then obtain

$$\frac{|\nabla T|}{|\nabla T|^{\mathrm{L}}} = \frac{\chi}{k_{\mathrm{B}}\rho^{\mathrm{L}}}\frac{dP_{\mathrm{s}}}{dT} \qquad (8)$$

with the mean gradient $|\nabla T| = \Delta T/L_x$ and the gradient in the liquid $|\nabla T|^{\mathrm{L}} = -[T(x_2^{\mathrm{int}}) - T(x_1^{\mathrm{int}})]/\Delta^{\mathrm{L}}$, where we have evaluated dP_{s}/dT at $T = T_{\mathrm{m}}$ [24].

Since $T(x)$ is continuous and heat flux is uniform, $|\nabla T|/|\nabla T|^{\mathrm{L}}$ is linear in X for $X_{\min} \leq X \leq X_{\max}$ when $\rho^{\mathrm{L}} \gg \rho^{\mathrm{G}}$. Then, the relation (8) indicates that X is a linear function of χ in $\chi_{\min} \leq \chi \leq \chi_{\max}$ [24], where

$$\chi_{\min/\max} = k_{\mathrm{B}}\rho^{\mathrm{L}}\left(\frac{dP_{\mathrm{s}}}{dT}\right)^{-1}\left[\frac{\Delta^{\mathrm{L}}}{L_x} + \frac{\kappa^{\mathrm{L}}}{\kappa_{2/1}^{\mathrm{G}}}\left(1 - \frac{\Delta^{\mathrm{L}}}{L_x}\right)\right]. \qquad (9)$$

κ^{L}, κ_1^{G}, and κ_2^{G} are heat conductivities of the liquid, the hot gas, and the cold gas, respectively. To be $\chi_{\min} < \chi_{\max}$, κ_2^{G} must be larger than κ_1^{G}. Consistently, $\kappa_2^{\mathrm{G}}/\kappa_1^{\mathrm{G}}$ is estimated about 2.5 at the hovering state of $\chi = 12.65$ and $\Delta^{\mathrm{L}} \simeq L_x/2$ for larger systems with $L_x/\sigma = 632$ and 1581 [24]. Using numerical estimates for ρ^{L} and dP_{s}/dT, the values of $\chi_{\min}$ and $\chi_{\max}$ are determined according to (9). The obtained graph $X = X(\chi)$ is shown in Fig. 3 as the dotted line, in which $\chi_{\min} = 7.8$ and $\chi_{\max} = 16$.

Last, we comment that the cold gas is thermodynamically unstable even in the macroscopic limit. For the gas to be stable, the condition $P(x) \leq P_{\mathrm{s}}(T(x))$ should be satisfied. Combining the force balance $P(x) - P_{\mathrm{s}}(T(x_2^{\mathrm{int}})) = -mg\rho^{\mathrm{G}}(x - x_2^{\mathrm{int}})$ in the cold gas with the Fourier law, we rewrite the stability condition as $-\kappa^{\mathrm{L}}|\nabla T|^{\mathrm{L}}(dP_{\mathrm{s}}/dT) \leq mg\rho^{\mathrm{G}}\kappa_2^{\mathrm{G}}$. We then eliminate $|\nabla T|^{\mathrm{L}}$ by substituting (8). Finally, using the definition of χ in (6), we obtain the stability condition for the cold gas as

$$\rho^{\mathrm{L}}\kappa^{\mathrm{L}} \leq \rho^{\mathrm{G}}\kappa_2^{\mathrm{G}}. \qquad (10)$$

This inequality is hardly reachable because $\rho^{\mathrm{G}} \ll \rho^{\mathrm{L}}$, and therefore, the cold gas is supercooled in general.

We here provide a physical explanation of how the cold gas becomes metastable [24]. First, the pressure at the interface is determined as the saturation pressure $P_{\mathrm{s}}(T(x_2^{\mathrm{int}}))$, and the pressure above the interface is kept almost constant owing to the low density of the gas. Second, according to the Fourier law, a small heat conductivity in gas results in a steep temperature gradient, and thus the upper region of the gas becomes colder than near the interface. The combination of these two facts leads to the result that the gas situated sufficiently above the interface can only be supercooled.

Summary and discussion—We numerically observed the floating up of a liquid against gravity by imposing heat flow. The liquid hovers steadily without separating into pieces. The hovering state is characterized by the scaling function of the dimensionless parameter χ. The cold gas situated above the liquid remains metastable and super-cooled. The phenomenon has been explained from the thermodynamic argument based on the saturation property at the two liquid-gas interfaces.

The most important achievement will be experimental observation of these phenomena. The scaling function $X(\chi)$ allows us to predict the temperature difference required for the floating up of the liquid against the gravity of the earth. As an example, we consider the conditions under which xenon floats up. The noble gas xenon shows liquid-gas coexistence around 220 K, where the mass density ratio between the liquid and gas is $\rho^{\mathrm{L}}/\rho^{\mathrm{G}} = 13$. Applying $X(\chi)$ in Fig. 3, the xenon in the container with $L_x = 1$ cm, $L_y = L_z = 0.25$ cm is expected to float up even with a small temperature difference of $\Delta T = 0.2$ K [24]. We thus believe that experimental observations are feasible. Not restricted to noble gases, familiar materials, such as nitrogens, carbon dioxide, and water can show the phenomenon, too. A possible difficulty is choosing a material for the container whose walls are repulsive to the fluid, such as the superhydrophobic materials used in the cold Leidenfrost examination for water [6]. The effect of boundary properties, including details of the thermostats, on the hovering phenomenon should be investigated further. Related to the experimental realization, a phenomenon that a slightly heavier phase is located above a lighter phase has been reported for liquid crystals in the heat conduction [26].

At the end of this Letter, we briefly discuss convection in macroscopic systems. The onset of thermal convection driven by the buoyancy force would be characterized by a threshold value of the Rayleigh number. Since the value of χ can be chosen independently of the Rayleigh number, the liquid hovering can occur in the absence of this type of convection. One may consider another mechanism of convection driven by the temperature dependence of the surface tension, called Marangoni convection. We conjecture that this mechanism does not work in liquid-gas interfaces, because the temperature modulation along the interface leads to evaporation or condensation processes, which inhibit the flow caused by the surface tension. Furthermore, even if convection occurs at a larger Rayleigh number than the threshold value, the hydrodynamic instability should be studied for the stationary hovering state when $\chi \geq \chi_{\min}$. That is, the phenomena reported in this Letter provide a starting point for more complex states.

[1] E. M. Agee, Mesoscale cellular convection over the oceans, Dyn. Atmos. Oceans, **10**, 317 (1987).

[2] H. D. Orville, A review of cloud modeling in weather modification, Bull. Am. Meteorol. Soc. **77**, 1535 (1996).

[3] T. Dror, I. Koren, H. Liu, and O. Altaratz, Convective steady state in shallow cloud fields, Phys. Rev. Lett. **131**, 134201 (2023).

[4] J. G. Leidenfrost, *De aquae communis nonnullis qualitatibus tractatus* (Duisburg, 1756).

[5] D. Quéré, Leidenfrost dynamics, Annu. Rev. Fluid Mech. **45**, 197 (2013).

[6] P. Bourrianne, C. Lv, and D. Quéré, The cold Leidenfrost regime, Sci. Adv. **5**, eaaw0304 (2019).

[7] J. Rodrigues and S. Desai, The nanoscale Leidenfrost effect, Nanoscale **11**, 12139 (2019).

[8] B. L. Holian and D. J. Evans, Shear viscosities away from the melting line: A comparison of equilibrium and nonequilibrium molecular dynamics, J. Chem. Phys. **78**, 5147 (1983).

[9] B. L. Holian and Dennis E. Grady, Fragmentation by molecular dynamics: The microscopic "big bang," Phys. Rev. Lett. **60**, 1335 (1988).

[10] W. Kob and H. C. Andersen, Scaling behavior in the β-relaxation regime of a supercooled Lenard-Jones mixture, Phys. Rev. Lett. **73**, 1376 (1994).

[11] J. J. Potoff and A. Z. Panagiotopoulos, Critical point and phase behavior of the pure fluid and a Lennard-Jones mixture, J. Chem. Phys. **109**, 10914 (1998).

[12] A. Røsjorde, D. W. Fossmo, D. Bedeaux, S. Kjelstrup, and B. Hafskjold, Nonequilibrium molecular dynamics simulations of steady-state heat and mass transport in condensation: I. Local equilibrium, J. Colloid Interface Sci. **232**, 178 (2000).

[13] B. Doliwa and A. Heuer, Hopping in a supercooled Lenard-Jones liquid: Metabasins, waiting time distribution, and diffusion, Phys. Rev. E **67**, 030501(R) (2003).

[14] F. Ogushi, S. Yukawa, and N. Ito, Asymmetric structure of gas-liquid interface, J. Phys. Soc. Jpn. **75**, 073001 (2006).

[15] T. Ishiyama, S. Fujikawa, T. Kurz, and W. Lauterborn, Nonequilibrium kinetic boundary condition at the vapor-liquid interface of argon, Phys. Rev. E **88**, 042406 (2013).

[16] S. K. Oh, Modified Lennard-Jones potentials with a reduced temperature-correction parameter for calculating thermodynamic and transport properties: Noble gases and their mixtures (He, Ne, Ar, Kr, and Xe), J. Thermodyn. **1**, 29 (2013).

[17] H. Watanabe, M. Suzuki, H. Inaoka, and N. Ito, Ostwald ripening in multiple-bubble nuclei, J. Chem. Phys. **141**, 234703 (2014).

[18] R. Holyst, M. Litniewskia, and D. l Jakubczykb, Evaporation of liquid droplets of nano- and micro-meter size as a function of molecular mass and intermolecular interactions: Experiments and molecular dynamics simulations, Soft Matter **13**, 5858 (2017).

[19] J. Muscatello, E. Chacón, P. Tarazona, and F. Bresme, Deconstructing temperature gradients across fluid interfaces: The structural origin of the thermal resistance of liquid-vapor interfaces, Phys. Rev. Lett. **119**, 045901 (2017).

[20] M. Heinen and J. Vrabec, Evaporation sampled by stationary molecular dynamics simulation, J. Chem. Phys. **151**, 044704 (2019).

[21] S. Stephan, M. Thol, J. Vrabec, and H. Hasse, Thermophysical properties of the Lennard-Jones fluid: Database and data assessment, J. Chem. Inf. Model. **59**, 4248 (2019).

[22] J. Wen, D. Dini, H. Hu, and E. R. Smith, Molecular droplets vs bubbles: Effect of curvature on surface tension and Tolman length, Phys. Fluids **33**, 072012 (2021).

[23] J. D. Weeks, D. Chandler, and H. C. Andersen, Role of repulsive forces in determining the equilibrium structure of simple liquids, J. Chem. Phys. **54**, 5237 (1971).

[24] See Supplemental Material at http://link.aps.org/supplemental/10.1103/PhysRevLett.133.117101 for detailed explanations, supplemental numerical data, parameters, and derivations, which includes Refs. [16,25].

[25] J. Irving and J. Kirkwood, The statistical mechanical theory of transport processes. IV. The equations of hydrodynamics, J. Chem. Phys. **18**, 817 (1950).

[26] S. Sakurai, A. Tschammer, W. Pesch, and G. Ahlers, Convection in the presence a first-order phase change, Phys. Rev. E **60**, 539 (1999).